

---

# A measurement of $G$ with a cryogenic torsion pendulum

Riley Newman, Michael Bantel, Eric Berg and William Cross

*Phil. Trans. R. Soc. A* 2014 **372**, 20140025, published 8 September 2014

---

## References

[This article cites 8 articles](#)

<http://rsta.royalsocietypublishing.org/content/372/2026/20140025.full.html#ref-list-1>

[Article cited in:](#)

<http://rsta.royalsocietypublishing.org/content/372/2026/20140025.full.html#related-urls>

## Subject collections

Articles on similar topics can be found in the following collections

[relativity](#) (13 articles)

## Email alerting service

Receive free email alerts when new articles cite this article - sign up in the box at the top right-hand corner of the article or click [here](#)



## Research

**Cite this article:** Newman R, Bantel M, Berg E, Cross W. 2014 A measurement of  $G$  with a cryogenic torsion pendulum. *Phil. Trans. R. Soc. A* **372**: 20140025.  
<http://dx.doi.org/10.1098/rsta.2014.0025>

One contribution of 13 to a Theo Murphy Meeting Issue ‘The Newtonian constant of gravitation, a constant too difficult to measure?’

### Subject Areas:

relativity

### Keywords:

$G$ , gravitational constant, Newton’s constant

### Author for correspondence:

Riley Newman

e-mail: [rdnewman@uci.edu](mailto:rdnewman@uci.edu)

# A measurement of $G$ with a cryogenic torsion pendulum

Riley Newman<sup>1</sup>, Michael Bantel<sup>1,2</sup>, Eric Berg<sup>1</sup>  
and William Cross<sup>1,3</sup>

<sup>1</sup>Department of Physics, University of California Irvine, Irvine, CA 92697-4575, USA

<sup>2</sup>ExoAnalytic Solutions Inc., Mission Viejo, CA 92692, USA

<sup>3</sup>MongoDB, New York, NY 10036, USA

A measurement of Newton’s gravitational constant  $G$  has been made with a cryogenic torsion pendulum operating below 4 K in a dynamic mode in which  $G$  is determined from the change in torsional period when a field source mass is moved between two orientations. The source mass was a pair of copper rings that produced an extremely uniform gravitational field gradient, whereas the pendulum was a thin fused silica plate, a combination that minimized the measurement’s sensitivity to error in pendulum placement. The measurement was made using an as-drawn CuBe torsion fibre, a heat-treated CuBe fibre, and an as-drawn Al5056 fibre. The pendulum operated with a set of different large torsional amplitudes. The three fibres yielded high  $Q$ -values: 82 000, 120 000 and 164 000, minimizing experimental bias from fibre anelasticity.  $G$ -values found with the three fibres are, respectively:  $\{6.67435(10), 6.67408(15), 6.67455(13)\} \times 10^{-11} \text{ m}^3 \text{ kg}^{-1} \text{ s}^{-2}$ , with corresponding uncertainties 14, 22 and 20 ppm. Relative to the CODATA2010  $G$ -value, these are higher by 77, 37 and 107 ppm, respectively. The unweighted average of the three  $G$ -values, with the unweighted average of their uncertainties, is  $6.67433(13) \times 10^{-11} \text{ m}^3 \text{ kg}^{-1} \text{ s}^{-2}$  (19 ppm).

## 1. Introduction

Our  $G$  measurement uses the ‘dynamic’ or ‘time of swing’ method, in which  $G$  is determined based on the change of torsional oscillation frequency of a pendulum when the configuration of gravitational field source masses is altered. This method has the

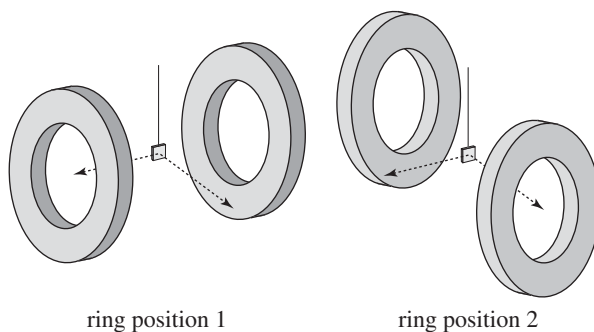


**Figure 1.** Diagram of source mass rings and the torsion pendulum in the two measurement positions  $90^\circ$  apart.

considerable advantage of requiring neither a calibrated reference force nor precision measurement of angular displacements. A potential drawback of the method is its susceptibility to systematic error arising from anelastic properties of the torsion fibre which suspends the pendulum. This danger was emphasized by Kuroda [1], who showed that a widely accepted model for linear anelastic behaviour, with reasonable parameter assumptions as investigated by Quinn *et al.* [2], leads to an upward fractional bias in a  $G$  measurement of  $1/(\pi Q)$ , where  $Q$  is the quality factor of the pendulum's torsional oscillation mode.

### (a) Features of our measurement

For our measurement, we use a thin-plate torsion pendulum and a pair of ring-shaped source masses separated by fused silica rods moved alternately between the positions indicated in figure 1. The gravitational interaction of the rings with the thin-plate pendulum has a form which makes the experiment extremely insensitive to error in the pendulum's position, size and mass distribution. Advantages of cryogenic operation include the following. (i) The pendulum  $Q$  is increased from a few thousand to over 100 000, reducing bias from the Kuroda mechanism to below 5 ppm. (ii) Thermal noise acting on the pendulum, which scales as  $\sqrt{k_B T/Q}$ , is reduced by nearly two orders of magnitude. (iii) The sensitivity of fibre properties, including its torsion constant, to temperature variation is greatly reduced. (iv) Excellent temperature control is easily maintained. (v) High vacuum is easily maintained. (vi) Highly effective magnetic shielding with superconducting lead becomes possible.

Our source mass system was necessarily positioned outside of the dewar, at the relatively large distance of 40 cm from the pendulum within the dewar. This large distance was an advantage in that it allowed a rapidly converging multipole treatment of the source mass–pendulum interaction and reduced sensitivity to non-uniformity of the rings' mass density, but the large distance meant that the magnitude of the signal torsional period change that must be measured (from 1.7 to 0.2 ms, depending on fibre material and oscillation amplitude) was many orders of magnitude smaller than that experienced in other 'dynamic'  $G$  measurements.

### (b) Extracting $G$ from data

A full formalism for analysing the behaviour of the pendulum and source mass system is presented in §4. Here, we outline the main features of the analysis.

The gravitational torque on a torsion pendulum may be expressed as

$$\tau(\theta) = - \sum_{\ell m} i m q_{\ell m} a_{\ell m}^* e^{-i m \theta}, \quad (1.1)$$

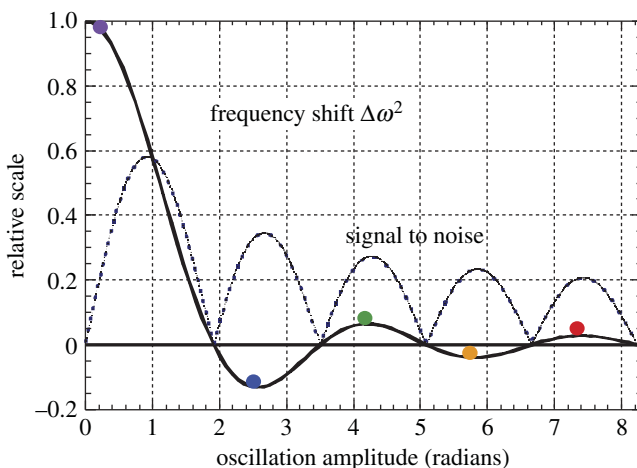


**Figure 2.** Relative signal strength, and signal-to-noise ratio, as functions of torsional amplitude. The five solid dots indicate torsional amplitudes near which the pendulum operated. (Online version in colour.)

where  $\theta$  is the angular displacement of the pendulum relative to the source mass distribution, the  $q_{\ell m}$  are mass multipole moments of the pendulum in a body-fixed coordinate system, the  $a_{\ell m}$  are determined by the source mass density distribution, and the sum is over all  $\ell > 0$  and  $|m| \leq \ell$ . The ring and rod combination generates a gravitational field characterized by  $a_{\ell m}$  which vanish for  $\ell = 1, 3, 4$  and  $5$ . This occurs for odd  $\ell$  by symmetry, and for  $\ell = 4$  as a result of a particular ring spacing. A consequence is that spatial derivatives of the field gradient vanish for order 1, 2 and 3 at the midpoint between the rings, so that the field gradient is extremely uniform over a large region centred on the pendulum. The torque on the pendulum is then almost purely from a coupling to its quadrupole moment  $q_{22}$ , and is given to high precision by

$$\tau = \pm 4|q_{22}a_{22}| \sin(2\theta), \quad (1.2)$$

where the minus and plus signs apply when the rings are in positions 1 and 2, respectively (figure 1). Solving the torsional equation of motion using equation (1.2) one finds that when the rings move from position 2 to 1 the pendulum's frequency shift is given by

$$\Delta\omega^2 = \frac{16J_1(2A)}{A} \frac{|q_{22}a'_{22}|G}{I}, \quad (1.3)$$

where  $I$  is the pendulum's moment of inertia,  $A$  is its torsional oscillation amplitude in radians,  $J_1$  is a Bessel function and  $a'_{22}$  is defined to be  $a_{22}$  calculated setting  $G = 1$ . The calculation of  $q_{22}$  and  $a'_{22}$ , using equations introduced in §4c, must take into account geometrical and density imperfections of the source mass, addressed in §§3a and 5a, and of the pendulum, addressed in §§3b and 5b. Equation (1.3) is correct to about 10 ppm without considering higher-order pendulum and field moments. Solving this equation for  $G$  yields its experimental value.

Note that the right-hand side of equation (1.3) is proportional to the ratio of the pendulum's quadrupole moment to its moment of inertia, a ratio that, as the width of the thin-plate pendulum goes to zero, goes to a dimensionless constant independent of the pendulum's shape and mass distribution. Using a thin-plate pendulum then greatly eases metrology demands, a feature first noted and exploited by Gundlach & Merkowitz [3].

The amplitude dependence  $J_1(2A)/A$  of the  $\Delta\omega^2$  signal is illustrated in figure 2, along with the expected signal-to-noise ratio which scales as  $J_1(2A)$ . To minimize systematic error from bias in amplitude determination, we normally started each data run with an amplitude just above an extremum of  $J_1(2A)/A$ , so that the average amplitude over the duration of a run was close to one of the extremum values indicated in figure 2. We eventually determined that our amplitude

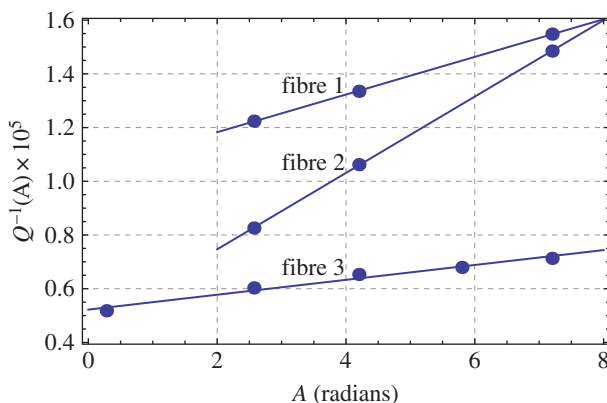


**Figure 3.** Measured dependence of pendulum  $Q^{-1}$  on torsional amplitude for the three fibres: no. 1 as-drawn CuBe, no. 2 heat-treated CuBe and no. 3 as-drawn Al5056. The linear amplitude dependence is characteristic of a stick-slip contribution to fibre energy dissipation. (Online version in colour.)

determination was accurate to a few microradians, good enough to allow safe operation near the 0.26 radian point indicated in figure 2.

### (c) Torsion fibres

Three types of fibres were used in the measurements, each about 250 mm long:

1. 20  $\mu\text{m}$  diameter alloy 25 CuBe as drawn.
2. 20  $\mu\text{m}$  diameter alloy 25 CuBe heat treated.
3. 25  $\mu\text{m}$  diameter Al5056 as drawn.

These and their corresponding datasets are referenced as fibres 1, 2 and 3 in the remainder of this paper.

Fibre stock was purchased from California Fine Wire. The heat treatment of fibre 2 was in vacuum at 320°C for 8 h, followed by slow cooling in vacuum at about 30°C per hour. Figure 3 shows  $Q^{-1}$  as a function of torsional amplitude, observed for these fibres when suspending the pendulums used in our  $G$  measurement.

We have shown [4] that, in the framework of the model treated by Kuroda [1] and Quinn *et al.* [2], fractional  $G$  error from anelasticity is, to order  $Q^{-1}$ , bounded between 0 and  $1/(2Q)$ . In this linear model,  $Q^{-1}$  is independent of the torsional amplitude of a pendulum. In preparation for our  $G$  measurement, we made extensive studies of torsion fibre properties at low temperature [5,6], finding that in fact fibres made of CuBe, tungsten and Al5056 all showed a large extremely linear variation of  $Q^{-1}$  with amplitude. The CuBe fibre most intensively studied exhibited behaviour strikingly consistent with the following predictions [5,7] of a stick-slip model: (i) linear dependence of  $Q^{-1}$  on amplitude, (ii) linear dependence of torsional frequency  $\omega^2$  on amplitude (after subtracting a contribution from a third-order  $k_3\theta^3$  elastic torque term, determined from measurements of a  $\sin(3\omega t)$  harmonic amplitude), (iii) a ratio  $(dQ^{-1}/dA)/(\omega^2/dA)$  within 2% of the value  $-4/3\pi\omega^2$  predicted by the stick-slip model, and (iv) a characteristic pointy ‘Davidenko’ [7] hysteresis loop close to that predicted by the model. The value of  $dQ^{-1}/dA$  was the same at 77 K as at 4.2 K, indicating temperature independence of this internal friction component, whereas the zero-amplitude intercept of  $Q^{-1}(A)$  increased by a factor of about 3.4 between 4.2 and 77 K. We established that the observed stick-slip behaviour was associated with the fibre and not the epoxy used to mount it at its ends, by making measurements at 77 K with a string of epoxy droplets along the fibre. Each such droplet should contribute the same amount to

**Table 1.** ppm correction  $\delta G_{\text{ppm}} = 1/(\pi Q)$  to be added to  $G$  (measured) found using the three fibres. The first column shows the correction actually used for each fibre:  $\delta G_{\text{ppm}}$  based on the  $Q^{-1}$  limit at zero torsional amplitude. The other columns indicate what  $\delta G_{\text{ppm}}$  would be if based on  $Q$  (amplitude  $A$ ). Uncertainties are taken to be half the magnitude of the correction.

fibre	$A = 0$	0.3	2.57	4.2	5.8	7.4
1	$-3.3 \pm 1.7$	-3.4	-3.9	-4.2	-4.6	-4.9
2	$-1.5 \pm 0.8$	-1.6	-2.6	-3.4	-4.1	-4.8
3	$-1.7 \pm 0.9$	-1.8	-1.9	-2.1	-2.2	-2.3

$Q^{-1}$  as the combined contribution of the epoxy mounting at the top and bottom of the fibre. The added droplets substantially increased the zero-amplitude intercept of  $Q^{-1}(A)$ , but did not affect the value of  $dQ^{-1}/dA$ . We concluded from this study that the CuBe fibre’s internal friction has two independent contributions:  $Q^{-1} = Q_I^{-1}(T) + Q_{II}^{-1}(A)$ , where  $Q_I^{-1}$  is temperature dependent but amplitude independent and arises from a linear mechanism, whereas  $Q_{II}^{-1}$  is temperature independent but amplitude dependent and arises from a stick–slip mechanism associated with the fibre. The stick–slip contribution to torque is found to be

$$-k_{ss}[(A^2 - \theta^2)\hat{\theta} - 2A\theta], \tag{1.4}$$

where  $\hat{\theta}$  is the direction of the angular velocity, and  $k_{ss}/k_1 = (3\pi/8)(dQ^{-1}/dA)$  where  $k_1$  is the first-order fibre torsion constant.

The stick–slip mechanism is frequency independent, so its contribution to the fibre’s torsion constant should not change when the pendulum’s oscillation frequency is altered by a change in orientation of the source masses. Thus, the stick–slip behaviour should not contribute to a Kuroda bias. Therefore, we took our Kuroda bias correction for each fibre to be  $dG = Q_0^{-1}/\pi$ , where  $Q_0^{-1}$  is the zero-amplitude value of a linear fit to  $Q^{-1}(A)$ , corresponding to the amplitude-independent (but frequency-dependent) contribution to  $Q^{-1}$  according to our analysis [6]. We assigned an uncertainty to each  $dG$  equal to half its magnitude. Table 1 shows the ppm  $dG$  correction (to be added to the uncorrected  $G$ -value) found in this way for the three fibres, and also shows the  $dG$  correction as a function of amplitude if based (we believe incorrectly) on the full amplitude. In all cases, the correction is less than 5 ppm.

## 2. Apparatus

The measurement apparatus operated in a former Nike missile bunker located on an arid-lands environmental preserve at Hanford in eastern Washington state, where microseismic background is very low. The site was managed by the Pacific Northwest National Laboratory (PNNL). Figure 4 is a scale drawing showing the size and relative positions of the source mass rings, the pendulum and the evacuated pendulum housing within a liquid helium dewar. The dewar was 46 cm in diameter, 290 cm in height and accommodated a 30 cm diameter insert; its helium-holding time was about 6 days. The dewar was mounted on a turntable; by periodically rotating the dewar in alternate directions, the torsional oscillations of the pendulum within it could be resonantly driven to any desired amplitude. By taking pendulum oscillation data at a set of dewar angular positions, the effects of gravitational and magnetic couplings of the pendulum to external field sources could be determined.

### (a) Source mass rings

The 59 kg rings were machined from C10100 99.99% purity half-hard OFHC copper, with nominal OD 520.7, ID 312.42 and thickness 48.26 mm. To minimize mass change owing to surface oxidation, the rings were plated with a 7.5  $\mu\text{m}$  non-magnetic coating of nickel with 8% phosphorus. The rings were machined and plated by the Los Alamos National Laboratory

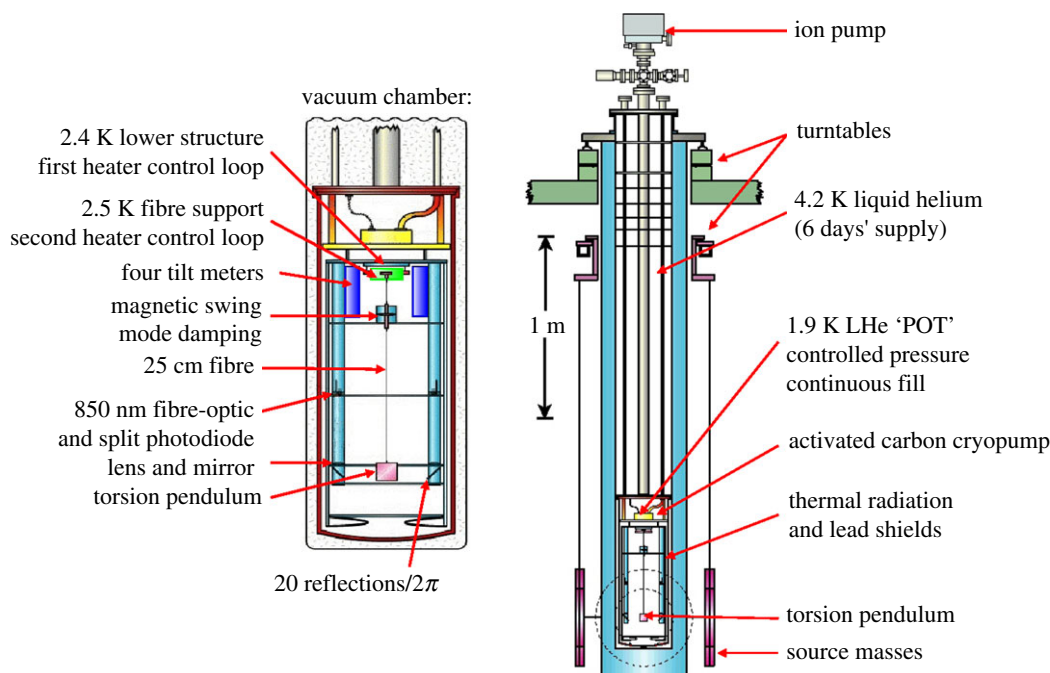


**Figure 4.** The cryostat and associated apparatus. (Online version in colour.)

(LANL). A dimensionally critical 650 mm spacing of the two rings was maintained by a pair of 8 mm diameter fused silica rods extending between them. The rings hung outside the dewar, suspended by a Kevlar string from a turntable 1.87 m above their centre. The turntable rotated the rings under computer control at intervals of about 30 min to modulate the gravitational signal. Stationary positions of the turntable were determined by detentes located at  $45^\circ$  intervals, with relative angular positions calibrated to within  $20\ \mu\text{rad}$  using a Heidenhain model 800 angular encoder. An optical lever that views mirrors on the turntable confirmed accurate arrival of the turntable at a detente, and if necessary provided a correction signal to the turntable. The turntable transport speed envelope was designed to bring the rings to rest without swinging at the end of a transport. The output of an optical lever viewing a small mirror on one of the rings allowed the turntable control system to actively damp residual swing motion. This swing signal was recorded for later analysis. A platinum resistor thermometer embedded in each ring monitored its temperature, supporting the calculation of correction for its thermal expansion.

## (b) Pendulum and torsion fibres

The pendulum was a 10.7 g Corning 7980-OAA fused silica plate, with dimensions  $40 \times 40 \times 3\ \text{mm}$ , made by General Optics Inc. The four sides of the pendulum were coated with a 100 nm layer of aluminium and a 27 nm layer of  $\text{SiO}_2$  by Newport Optics. Two similar pendulums were used in the course of the project. In later years, an additional coating was applied to the second pendulum, adding 5 nm of chromium and 200 nm of gold, to improve its reflectivity and thus reduce heat absorption. The pendulum suspension had two stages: an upper phosphor-bronze fibre,  $380\ \mu\text{m}$  in diameter and 73 mm long, which suspended an aluminium damping disc between a pair of ring magnets, and the main 250 mm long fibre which extended from this disc down to the pendulum. Eddy current damping in the disc served to damp swinging modes of the pendulum without significantly reducing the mechanical  $Q$  of the torsional oscillation mode. The torsion fibres were mounted with Stycast1266 epoxy in 1.6 mm diameter 20 mm long aluminium ferrules which were clamped to support the fibre upper end and tapped



at the lower end to thread onto a 00-90 threaded brass rod epoxied with Stycast1266 in a hole in the top of the pendulum plate. Prior to mounting, the fibres were hand polished successively with 1.0, 0.3 and 0.05  $\mu\text{m}$  aluminium oxide grit in water and cleaned with acetone and ethanol.

### (c) Cryostat temperature control

Figure 4 shows details of the pendulum temperature control system and optics within the vacuum chamber in which the pendulum operates. Three levels of temperature control were normally maintained. A secondary helium chamber, thermally isolated from the vacuum chamber walls, drew helium through a capillary tube from the main dewar chamber. Controlled pumping of this chamber maintained it at a constant temperature near 2 K. The chamber was thermally coupled to a cylindrical aluminium shell with 3 mm walls. Within this shell, an inner framework was mounted with thermally isolating legs and maintained at a constant slightly higher temperature by a sensor/heater PI control system. Finally, the pendulum was suspended from a small platform mounted with thermally isolating legs to the inner framework which was maintained at constant temperature by a second sensor/heater control system. The temperature at which this pendulum suspension point was maintained was different at various stages of the project, at set points between 2.4 and 3.1 K except for runs made in y2000 with fibre 2 in which the temperature set point was near 4.6 K. The performance of the cryostat temperature control system was progressively improved; throughout the data runs of y2006, the suspension point temperature was typically maintained within  $\pm 10 \mu\text{K}$  for periods of a day or more. There was however evidence of temperature variation at the fibre suspension point correlated with the source mass position, a source of systematic error discussed in §5c(ii).

### (d) Source mass temperature

The temperature of the source mass was uncontrolled. It ranged from 18.7°C to 23.9°C in y2000, when fibre 1 data and half of the fibre 2 data were obtained, from 17.0°C to 18.3°C during y2002 when the balance of fibre 2 data was obtained, and from 19.0°C to 19.8°C in y2006 when fibre 3 data were taken. A 100 ohm platinum thermometer (Lake Shore PT-111) was mounted with grease in a small hole in each ring. We calibrated these thermometers at the temperatures of melting ice and melting gallium using a gallium calibration kit obtained from the National Institute of Standards and Technology (NIST). The thermometers monitored ring temperatures both during dimensional metrology at the NIST and during  $G$  data runs. The sensitivity of source field strength to ring temperature determinations is  $-30.77 \text{ ppm K}^{-1}$ . Uncertainty in ring temperature measurement contributes 1.5 ppm to our uncertainty budget.

### (e) Optical readout

Four independent optical levers viewed the pendulum, positioned at 90° intervals about the torsion fibre axis. Two of these are visible in figure 4. The four optical systems are identical in their mass distribution, to ensure fourfold mass symmetry about the pendulum. Only one of the optical levers was used in practice. A set of eight stationary mirrors surrounded the pendulum, at angles 20°, 70°, 110° and 160° on each side relative to the optical axis of an optical lever. A 62.5  $\mu\text{m}$  core optical fibre delivered the light of a Honeywell HFE4226-022 850 nm LED at room temperature to the focal plane of the optical lever. Light emitted at this point was collimated by a 163 mm focal length lens below, and directed towards the pendulum by a mirror. When one of the pendulum's faces was in one of a set of angular positions this light was reflected, either directly or after reflection from one of the surrounding stationary mirrors, back through the same path. The resulting imaged spot swept past a Centronic LD2A-0 PIN two-element photodiode in the lens focal plane just beside the end of the optical fibre. The amplified differential signal from the spot transit was digitized in the region of the zero crossing at intervals of (typically) 2  $\mu\text{s}$ , and fitted to a third-order polynomial whose zero gave a precise measure of the time of the transit. To



minimize heating of the pendulum by absorbed light power, the LED light source was normally activated only for the few milliseconds during which it could provide useful information.

## (f) Magnetic shielding

The pendulum was surrounded by two layers of superconducting lead shielding in the cryogenic environment. One layer was on the outer surface of the vacuum chamber, and another on the outside surface of an internal 3 mm thick aluminium cylinder surrounding the pendulum. Wrapped about the outside of the dewar was a high-permeability shield made of overlapping strips of 'Metglas', a commercial very-high-permeability amorphous ferromagnetic alloy. A decaying alternating electrical current in copper strips wound in toroidal fashion about the Metglas layer was applied before cooling the apparatus, to optimize the Metglas layer's shielding of external magnetic fields. The effectiveness of this combination of magnetic shields was tested with a special pendulum to which was attached a tiny calibrated magnetic dipole with magnetic moment  $(9.4 \pm 2) \times 10^{-6} \text{ J T}^{-1}$ . A measurement of the torsional period modulation produced by a rotating permanent magnet outside the dewar indicated the strength of the B field penetrating the cryogenic environment of the pendulum which, when compared with a measurement of the B field modulation amplitude at a corresponding distance in air, indicated a shielding factor of about 2000.

## 3. Dimensional and mass metrology

### (a) Gravitational field sources

*Ring dimensional metrology.* Dimensional metrology of the rings was performed by the NIST at Gaithersburg, with accuracy estimated by the NIST to be  $0.5 \mu\text{m}$  at a 90% confidence level. OD and ID measurements were made at five axial positions. Thickness was measured over a range of azimuthal and radial positions that covered roughly two-thirds of the ring surface. (Here 'axial, azimuthal and radial' represent coordinates characteristic of the symmetry of the rings as measured at the NIST, not coordinates defining their later placement in the experimental apparatus.) All these measurements were later supplemented at the University of California Irvine (UCI) using a Federal electronic differential gauge probe. When normalized to agree with the NIST measurements where available, the Irvine measurements extended OD, ID and thickness dimensional metrology to essentially all parts of the rings. Mass and mean dimensional values for the rings are presented in table 2. The rings were found to taper in thickness from inside to outside radius, by about  $14 \mu\text{m}$  for one ring and  $10 \mu\text{m}$  for the other. The resulting source field differed by 24 ppm from that calculated for an ideal ring geometry with the same average thickness. The rings were suspended by Kevlar strings positioned on each ring by a machined groove. The size of this groove, and of OD and ID ring chamfers, was determined using a toolmaker's microscope to digitize images of slices of castings made of these features at multiple azimuthal positions, using a stable casting compound.

*Ring density inhomogeneity.* A set of 17 cylindrical 16 mm diameter coupons was taken symmetrically from the outside and inside portions of the stock from which one of the rings was cut. The relative densities of the coupons associated with this ring were determined by weighing them in air and in 'Fluorinert' FC-77, a liquid with density  $1.75 \text{ g cm}^{-3}$  and high thermal conductivity. Relative densities were measured to about 5 ppm. The 17 measured coupon densities indicated a roughly linear density variation of about 13 ppm over the diameter of the ring. This variation would alter the calculated ring field moments by 0.2 ppm. The nickel plating thickness was estimated by LANL on the basis of plating duration to be  $7.5 \mu\text{m}$ . The calculated effect of this plating on the source field was  $(0.5 \pm 0.3) \text{ ppm}$ .

*Ring suspension issues.* Ideally, the rings hang in a plane perpendicular to the axis separating them. At the end of the project, measurements of the pattern of the turntable holes from which the rings were suspended revealed that the rings hung twisted around a vertical axis from the ideal

**Table 2.** Ring masses and averaged dimensional parameters. The parameters  $D_{ij}$  are the distances between the outside faces of four pairs of sapphire plates on opposite sides of a ring. These parameters together with rod lengths determine the distance of the effective ring midplane to the pendulum after averaging over ring configurations.

	ring 1	ring 2
mass (g)	58 704.38(24)	58 719.68(22)
averaged inner radius (mm)	156.1932(5)	156.1954(5)
averaged outer radius (mm)	26.3665(5)	260.3620(5)
averaged width (mm)	48.2610(5)	48.2561(5)
$D_{15}$ (mm)	48.2361(5)	48.2341(5)
$D_{26}$ (mm)	48.2427(5)	48.2399(5)
$D_{37}$ (mm)	48.2396(5)	48.2352(5)
$D_{48}$ (mm)	48.2336(5)	478.2356(5)

by about 3 mrad. This, together with uncertainty in the exact position of the suspension strings passing through their turntable guide holes, led to a source field correction of  $(10.7 \pm 4)$  ppm. Measurements were made to put a limit on the distortion of the rings' circular figure as they hang suspended from above. These put a limit of 0.5 ppm on the effect of such distortion.

*Averaging over ring configurations.* To reduce the effect of axial or azimuthal variation in ring dimensions and density, we made  $G$  data runs with the four different ring configurations produced by rotation of each ring in the pair by  $180^\circ$  about its vertical symmetry axis and/or by rotation by  $90^\circ$  about its horizontal symmetry axis. The original plan was to make a roughly equal number of data runs with each of these four configurations, for each fibre and each torsional amplitude, and then make an unweighted average of  $G$ -values found in each case. In practice, finding the task of changing ring configurations and ensuring that the reconfigured rings were suspended at the correct heights to be very awkward, error-prone and time-consuming, we chose to take data with a complete set of configurations only for runs with torsional amplitude in the 2.57 radian region, and only for fibres 1 and 2. The values  $G_n$  thus found for the four configurations served to determine a correction  $\bar{G} - G_n$  to be added to all runs using fibre 3, which used only one of the four configurations.

Using the averaging sequence to be described in §6*a*, no explicit ring configuration corrections were required in determining  $G$  using fibres 1 and 2. However, corrections were required to determine  $G$  separately from fibre 1 and 2 data taken at different torsional amplitudes, as will be displayed in figure 5. The average magnitude of the corrections thus applied was about 13 ppm.

*Ring mass determination.* Ring masses were measured by the NIST, with uncertainty about 4 ppm for each ring. The measured masses of the two rings differed by 261 ppm. One check of ring mass and dimensional metrology is afforded by comparing the resulting calculated densities of the two rings, which were found to differ by only 11 ppm—a difference that would be fully accounted for, for example, if the densities of the rings were actually identical and the average thickness of one of the rings was mis-measured by  $0.5\text{ }\mu\text{m}$ , whereas all other mass and dimensional measurements were exactly correct.

*Ring-spacing rods.* The critical separation distance of the rings was maintained by a pair of 73 g fused silica rods. These were 8 mm in diameter with approximately hemispherical ends. The rods reduced the quadrupole source mass field by about 0.3%. Careful measurements of the deviation from exact hemispherical form of the rod ends and of variation in rod diameter along its length led to field corrections of  $(3.0 \pm 1)$  and  $(0.3 \pm 1)$  ppm, respectively. Rod lengths were determined relative to a NIST-calibrated Invar ball bar, with corrections for temperature. Between the runs of y2000 and y2002, additional rod length comparisons were made with the reference bar using a sliding procedure which slightly abraded the rod ends, reducing their length by  $(2.1 \pm 1.5)\text{ }\mu\text{m}$ .

Eight sapphire plates, 5 mm in diameter and 1 mm thick, were glued in machined pockets in each ring. These served as bearing points for the fused silica rods that maintain the critical separation of the two rings. Four plates were set near the periphery of each ring at  $90^\circ$  intervals on each face, opposite a counterpart plate on the far face. A critical dimensional measurement is of the separation between sapphire plate surfaces on opposite sides of each ring, as this distance determines the average ring separation when the rings are rotated around a vertical axis between sets of data runs. NIST measurements of this separation, made on a grid of nine locations on each plate pair, served to determine not only the mean plate separation but also the amount by which each plate deviated from being perpendicular to the fused silica ring rods. The latter information, along with measurements of deviation from axial symmetry of the rounded rod ends, served to put limits on ring separation variation associated with rod rotation around the rod axes. These limits imply corresponding source field uncertainty at a level of about 0.5 ppm.

Contact between the rings and the rods which separate them was ensured by (i) suspending the rings so that their separation in the absence of the rods was slightly less than the rod length, while also (ii) slightly pressing the rings towards the rods using a loop made mainly of thread but including also two elastic rubber segments. This loop surrounded the ring pair at mid-height. Measurements of rod length change in response to compressional force, together with estimates of the compressional force, enabled an estimate of resulting  $G$  correction which was found to be negligible. Various versions of the elastic loop were used in different years of the  $G$  measurement programme, with correspondingly varying contributions to source field strength—typically a 15 ppm contribution, with about 0.6 ppm uncertainty.

### (i) Other gravitational field sources

*Co-moving with the source mass.* Section 5 lists the effects on field strength of items such as Delrin pins set into the rings to support and position the rods, and the platinum thermometers and associated readout wires. Objects at the level of the turntable that rotates the rings either have a fourfold symmetry, and thus do not contribute to the signal field, or have too little mass to contribute significantly.

*Laboratory fixed.* Section 5*d* discusses the small effect that a constant laboratory-fixed gravitational field gradient has on the pendulum's torsional frequency change when the source ring system rotates. To minimize this effect, approximately 11 tonnes of lead were placed in three stacks surrounding our apparatus, in a fashion designed to largely null the ambient gravitational field gradient arising from mass asymmetry in our underground laboratory and from a nearby mountain. Measurements of the residual static gravitational field gradient were made based on data taken with our apparatus in each of eight equally spaced angular orientations relative to its environment. This indicated background field gradients with magnitude less than 10% of the magnitude of the gradient generated by our source masses. Although careful measurements of this kind were made infrequently, estimates of the maximum gradient change that could arise from moved equipment in the laboratory or from rainfall were well below 10% of the signal. The sign and magnitude of the effect on our  $G$  measurement of the measured background gradients vary depending on the amplitude of the pendulum's torsional oscillation, but have a net effect on the measured  $G$  of each fibre of about  $(0 \pm 1)$  ppm.

### (b) The pendulum

Two nearly identical pendulums were used in this work, each with nominal dimensions: width and height 40.64 mm, thickness 3.00 mm. Mass and dimensional data for the pendulums are presented in table 3. Each edge was chamfered, with 0.4 mm projected width on each face. To couple the pendulum to its supporting fibre a 0.0422 g 00-90 brass rod was epoxied into a 1 mm diameter 4 mm deep hole centred on the top surface of the pendulum. This threaded rod engaged a tapped aluminium ferrule, 1.6 mm OD and about 14 mm long, into which the fibre was epoxied. As discussed in §1*b*, the interaction of the pendulum with the source mass

**Table 3.** Pendulum masses and primary dimensions.

	pendulum 1	pendulum 2
SiO <sub>2</sub> mass (g)	10.5966(1)	10.6536(1)
coating mass (g)	0.000835(150)	0.013761(200)
width (mm)	40.5902(1)	40.6375(1)
height (mm)	40.5900(1)	40.6159(1)
thickness (mm)	2.9430(4)	2.9558(4)

is almost completely determined by its ratio  $q_{22}/I$ , which is very weakly dependent on the pendulum's dimensions, and, except for small corrections for its plating and embedded brass screw, independent of its mass. Width and height measurements of the pendulum were made with a toolmaker's microscope. The most critical measurement was of the pendulum's thickness: the sensitivity of  $q_{22}/I$  (and hence of  $G$ ) is  $7.3 \text{ ppm } \mu\text{m}^{-1}$ . An electronic differential gauge was used to compare the thickness of each pendulum at multiple positions with the thickness of gauge blocks manufactured to nearly match the average pendulum thickness. Our estimated uncertainty in the pendulum thickness measurement is  $0.4 \text{ } \mu\text{m}$ , implying a  $2.9 \text{ ppm}$  uncertainty in  $q_{22}/I$ . Based on our mass and dimensional measurements, the densities of our two unplated fused silica pendulums were  $2.19455$  and  $2.19431 \text{ g cm}^{-3}$ , differing by only  $110 \text{ ppm}$ —a difference that would arise, for example, if the thickness of one of the pendulums had been mismeasured by  $0.3 \text{ } \mu\text{m}$ , with all other mass and dimensional measurements perfectly accurate.

## 4. Formal analysis framework

### (a) The pendulum's equation of motion

Define  $\theta$  and  $\dot{\theta}$  to be, respectively, the angular position and velocity of the pendulum relative to its equilibrium position. Torques that act on our pendulum as it rotates, in addition to that produced by our source mass, have several origins.

1. Nonlinear elastic torques associated with the fibre, which we may approximate with a Taylor series expansion:  $\tau = -(k_1\theta + k_2\theta^2 + k_3\theta^3)$ . Symmetry suggests that  $k_2$  should be zero, but in fact we have found significant non-zero values for this term in our tests. Fortunately,  $k_2$  proves to have negligible effect on our results.  $k_3$  however does have a marginally significant effect.
2. Dissipative fibre torques. As discussed in §1, these clearly seem to have two distinct contributions, one from the linear model discussed by Kuroda [1] and Quinn *et al.* [2], which has a very significant effect on the  $G$  measurement, and also a contribution from a stick-slip mechanism of unknown origin which produces a torque term  $-k_{ss}[(A^2 - \theta^2)\dot{\theta} - 2A\theta]$ .
3. Dissipative torques owing to magnetically induced eddy currents and residual gas damping. These are negligible compared with internal fibre dissipative torque, as the pendulum is non-conductive fused silica while the cryogenic environment together with a charcoal cryopump ensures extremely low gas pressure.
4. Torques with  $2\pi$  periodicity in the angular position of the pendulum, associated with static electric, magnetic and gravitational couplings of the pendulum to its environment. The sum of these torques may be represented by a Fourier expansion in the rotation angle  $\theta$ :  $\tau = -\sum_{m=1}^{\infty} \alpha_m \cos(m\theta) - \sum_{m=1}^{\infty} \beta_m \sin(m\theta)$ .

The torques discussed above imply an equation of motion,

$$I\ddot{\theta} = - \left[ k_1\theta + k_2\theta^2 + k_3\theta^3 + b\dot{\theta} + k_{ss}((A^2 - \theta^2)\hat{\theta} - 2A\theta) + \sum_{m=1}^{\infty} \alpha_m \cos(m\theta) + \sum_{m=1}^{\infty} \beta_m \sin(m\theta) \right]. \quad (4.1)$$

Here, a damping term  $b$  is included to roughly represent energy dissipation from the linear damping contribution, and  $k_{ss}/k_1 = (3\pi/8)(dQ^{-1}/dA)$ .

A solution of equation (4.1), correct to first order in the small ratios of  $k_2$ ,  $k_3$ ,  $\alpha_m$  and  $\beta_m$  to the dominant constant  $k_1$ , yields

$$\begin{aligned} \theta(t) = & A \sin(\omega t) - \frac{1}{6} A^2 \frac{k_2}{k_1} (3 + \cos(2\omega t)) - \frac{1}{32} A^3 \frac{k_3}{k_1} \sin(3\omega t) \\ & + \sum_{n=2,4,\dots}^{\infty} \left( \sum_{m=1}^{\infty} \frac{2J_n(mA)}{n^2 - 1} \frac{\alpha_m}{k_1} \right) \cos(n\omega t) + \sum_{n=3,5,\dots}^{\infty} \left( \sum_{m=1}^{\infty} \frac{2J_n(mA)}{n^2 - 1} \frac{\beta_m}{k_1} \right) \sin(n\omega t) \\ & - \sum_{m=1}^{\infty} J_0(mA) \frac{\alpha_m}{k_1} \end{aligned} \quad (4.2)$$

and

$$\omega^2 = \omega_0^2 \left( 1 + \frac{3}{4} A^2 \frac{k_3}{k_1} - 2 \frac{k_{ss}}{k_1} A + \frac{2}{A} \sum_{m=1}^{\infty} J_1(mA) \frac{\beta_m}{k_1} \right), \quad (4.3)$$

where

$$\omega_0^2 = \frac{k_1}{I}. \quad (4.4)$$

## (b) Testing the adequacy of these calculations

The effect of moving the source mass system between its two positions is to change the sign of its contribution to  $\beta_2$  and  $\beta_6$  (and to higher-order terms which may be neglected).

For the small values of  $k_3$ ,  $k_{ss}$ ,  $\alpha_m$  and  $\beta_m$  encountered in this work, the above solutions are sufficiently accurate for a determination of  $G$  to within about 10 ppm. To this order these terms, including the  $\alpha_m$ , and  $\beta_m$  from magnetic and gravitational couplings not associated with the source masses, do not affect the measured change in torsional frequency  $\Delta\omega^2$  when the signs of  $\beta_2$  and  $\beta_6$  are reversed.

However, two concerns arise

1. In the next order, not readily calculated, terms would appear in the expression for  $\omega^2$  proportional to the product of coefficients such as  $k_3$ ,  $k_{ss}$ ,  $\alpha_m$  times the relatively large part of the  $\beta_2$  coefficient associated with the source mass interaction. These terms will affect measured  $\Delta\omega^2$  values.
2. In extracting  $G$  from data using equation (4.3), it is critical that the amplitude  $A$  be measured accurately. Amplitudes are determined experimentally from the times at which reflections from mirrors at certain calibrated angular positions are registered. These positions are calibrated in separate runs, using their reflection times together with those from accurately known angles corresponding to  $\pm\pi$  or  $\pm 2\pi$  radians. These calculations are made assuming that the oscillatory motion of the pendulum has no harmonics. The harmonics are indeed extremely small—for example, at an amplitude  $A = 2.6$  radians the dominant harmonic, a  $\sin(3\omega t)$  component generated by the signal  $\beta_2$  term, has an amplitude of only  $2\ \mu\text{rad}$ . But it was important to determine the effect of harmonics on reflection angle calibration and application.

A powerful tool in exploring these issues proved to be numerical integrations of the equation of motion (4.1) to produce oscillatory functions that were then analysed with the same procedures

used to determine amplitudes and experimental values of  $\beta_2$  in analysing our actual  $G$  data. These integrations were made using MATHEMATICA, with WorkingPrecision and AccuracyGoal typically set to 400 and 20, respectively. Several tests of the accuracy of these integrations were made. In one test, equation (4.1) was integrated setting  $I$  and  $k_1$  equal to values corresponding to our apparatus,  $\beta_2$  equal to  $\pm\beta_{2S}$  (the values generated by our source mass) and the remaining torque components set to zero. The difference  $\Delta\omega^2$  between  $\omega^2$  found with  $+$  and  $-\beta_{2S}$  should agree extremely well with that calculated using only our first-order solution to equation (4.1), because second-order corrections to  $\omega^2$ , proportional to  $(\beta/k)^2$ , cancel in forming  $\Delta\omega^2$ . In fact,  $\Delta\omega^2$  with our simulation differed from the first-order prediction only by a fractional amount  $3 \times 10^{-10}$ . That difference divided by  $\omega^2$  was of the order of  $10^{-15}$ . Having established the reliability of our integration simulation technique with this and other tests, we then applied the technique to determine the corrections required for the many extra small torque terms in the full equation of motion. Results of this work are presented in §5d(ii).

### (c) Multipole expansion of the gravitational torque acting on the pendulum

We discuss here the vertical component of the torque on a pendulum of density  $\rho_{\text{pendulum}}(r, \theta, \phi)$  in a potential field  $\Phi(r, \theta, \phi)$  generated by external masses with density  $\rho_{\text{source}}(r, \theta, \phi)$ , where the polar coordinates  $r, \theta$  and  $\phi$  are centred on the pendulum's centre of mass with the polar axis vertical. The mass multipole moments of the pendulum are as conventionally defined

$$q_{\ell m} = \int \rho_{\text{pendulum}}(\mathbf{r}) r^\ell Y_{\ell m}^*(\theta, \phi) d^3\mathbf{r}. \quad (4.5)$$

Define gravitational field moments  $a_{\ell m}$  to be the coefficients in an expansion of the potential owing to the source masses,

$$\Phi_{\text{ext}}(r, \theta, \phi) = \sum_{\ell=0}^{\infty} \sum_{m=-\ell}^{\ell} a_{\ell m}^* r^\ell Y_{\ell m}^*(\theta, \phi). \quad (4.6)$$

(The  $a_{\ell m}$  so defined are proportional to the  $Q_{\ell m}$  used by Gundlach and Merkowitz in analysing their  $G$  measurement [3].) Then, for a field obeying Newton's law one can show that

$$a_{\ell m} = \frac{-4\pi G}{2\ell + 1} \int \frac{\rho_{\text{source}}(\mathbf{r})}{r^{\ell+1}} Y_{\ell m}^*(\theta, \phi) d^3\mathbf{r}. \quad (4.7)$$

One can then show that if the pendulum is rotated by an angle  $\theta$  relative to the frame in which  $q_{\ell m}$  was calculated, then the potential energy of the system is given by

$$U = \sum_{\ell=0}^{\infty} \sum_{m=-\ell}^{\ell} a_{\ell m}^* q_{\ell m} e^{-im\theta}. \quad (4.8)$$

The torque on the pendulum is

$$\tau_z(\theta) = -\frac{dU}{d\theta} = \sum_{\ell=1}^{\infty} \sum_{m=-\ell}^{\ell} i m a_{\ell m}^* q_{\ell m} e^{-im\theta}. \quad (4.9)$$

Using the symmetries of  $Y_{\ell m}$  on  $m \rightarrow -m$  in the expressions for  $q_{\ell m}$  and  $a_{\ell m}$ , we may write equation (4.9) in terms of a sum over positive  $m$ -values only,

$$\tau_z(\theta) = \sum_{\ell=1}^{\infty} \sum_{m=1}^{\ell} \text{Re}[2 m a_{\ell m}^* q_{\ell m} e^{-im\theta}]. \quad (4.10)$$



Comparing this with

$$\tau(\theta) = - \sum_m \alpha_m \cos(\theta) - \sum_m \beta_m \sin(\theta) \quad (4.11)$$

we find

$$\left. \begin{aligned} \alpha_m &= 2m \sum_{\ell \geq m} \text{Im}(a_{\ell m}^* q_{\ell m}) \\ \beta_m &= -2m \sum_{\ell \geq m} \text{Re}(a_{\ell m}^* q_{\ell m}). \end{aligned} \right\} \quad (4.12)$$

We calculate  $a_{\ell m}$  and  $q_{\ell m}$  assuming that the normal to the pendulum face in its equilibrium state is parallel to the symmetry axis of the ring source mass system. In that case,  $a_{\ell m}$  and  $q_{\ell m}$  are both real if pendulum, rings and rods have their ideal symmetric shape. If the pendulum's normal makes a small angle  $\phi_0$  with the ring axis, each  $\beta_m$  is reduced by a factor  $\cos(m\phi_0)$ . Because the interaction is dominated by  $m = 2$  terms, an undetected  $\phi_0$  produces a fractional  $G$  error  $\delta G \approx 2\phi_0^2$ . It is impossible to measure the pendulum's equilibrium orientation in its cryogenic environment directly, but  $\phi_0$  may be measured and made zero by rotating the cryostat to find an angle at which the  $\Delta\omega^2$  signal from ring transport vanishes, and then rotating the dewar back by  $\pi/4$  degrees. This was done whenever a new fibre was installed. From  $G$  data taken subsequently, the residual  $\phi_0$ -value could be determined from the difference in pendulum equilibrium position for the two source mass positions. That difference arises from the last term in equation (4.2), which is proportional to  $\alpha_2$ , which in turn is proportional to  $\phi_0$ .

#### (d) Extracting $G$ from frequency $\Delta\omega^2$ data

The significant frequency shift contributions when the rings are transported come from  $\beta_2$  (the sum of its  $\ell = 2, 4$  and  $6$  components) and  $\beta_6$  from  $\ell = 6$ . The relative contribution of  $\beta_6$  is amplitude dependent, but is less than 1.5 ppm at all amplitudes explored except at  $A \approx 0.3$ , where it is about 6 ppm. We ignore its contribution in initial analysis stages, and take it into account as a final correction to  $G$ -values. Noting that  $\omega_0^2 = k_1/I$ , we then find that without  $\beta_6$  equation (4.3) yields the first-order expression for  $\Delta\omega^2$ ,

$$\Delta\omega^2 = \frac{4}{AI} J_1(2A) \beta_2. \quad (4.13)$$

Now, remove the primary amplitude dependence from this equation by defining

$$S_0 \equiv \frac{A}{2J_1(2A)} \Delta\omega^2. \quad (4.14)$$

In an ideal world, we would have  $S_0 = K_0 G$  with  $K_0 = 2\beta_2(\text{ideal})/I$ , where  $\beta_2$  is evaluated with  $G = 1$  and for an idealized uniform source mass geometry (no chamfers, imperfections, etc). But there are many corrections that need to be made to this equation—for example,  $\beta_2$  is altered by chamfers, variations in ring temperature and air density, and corrections must be made for second-order terms proportional to  $k_3, k_{ss}, \beta_1$ , the 'Kuroda bias', etc. Our procedure was to apply to  $K_0$  all corrections, such as for chamfers or ring suspension strings, that remained constant in the course of all our data runs, and to apply to  $S_0$  those corrections which varied with time, such as ring temperature, and corrections, such as for 'Kuroda' bias, which depend on the fibre used. Then, if  $S$  and  $K$  represent the corrected versions of  $S_0$  and  $K_0$ , we have

$$S = KG, \quad (4.15)$$

where ideally all  $S$ -values found from individual 'aba' source mass round trip moves, as well as all averages of  $S$  over runs, fibre used, or amplitude should be the same.



**Table 4.** Corrections to  $K_0$  associated with the source mass, and  $K$  uncertainty from average ring mass and rod length uncertainties.

basis of change	$\Delta K$ (ppm)	uncertainty (ppm)
outer radius ring chamfers	36.2	0.9
inner radius chamfers	−28.7	0.8
slot for suspension string	140.1	1.8
ring width taper $w(r)$	24.2	1.0
NiP plating	0.5	0.25
rod contact sapphire plates	−3.2	0.01
plate mounting glue	−0.6	0.02
plate pockets	13.7	0.3
plate surface depression	34.6	3.5
rod positioning pins	1.4	0.01
pin pockets	10.7	0.7
hemispherical rod ends	−15.2	0
deviation from hemispherical ends	3.0	1.0
Kevlar suspension strings	19.4	0.1
y2000 rod–ring tensioner <sup>a</sup>	−20.1	0.6
holes for Pt thermometers	2.2	0.1
Pt thermometers	0.9	0.15
thermometer leads	0.4	<0.1
mirror for swing monitor	1.0	0.02
rod radius variation $r(x)$	0.3	1.0
suspension misalignment	10.7	4.0
$\ell$ , $m$ 4,2 and 6,2 contribution to $\beta_2$ <sup>b</sup>	3.8	0
ring mass	—	3.9
ring dimensions	—	2.8
total $\Delta K$ and uncertainty	235.6	7.8

<sup>a</sup>Yearly differences in tensioner contribution are incorporated in changes to  $S$ .

<sup>b</sup>The  $\ell m$  4,2 and 6,2 contribution to  $K$  was not included in  $K_0$ .

5. Transition from  $S_0$  and  $K_0$  to  $S$  and  $K$ , and systematic uncertainties

(a) Source mass corrections to  $K_0$

Table 4 indicates changes to the value of the  $K_0$  which was computed using the dimensional parameters in table 2. The tabulated changes correspond to deviations of the field source rings and rods from an idealized perfect cylindrical symmetry.

(b) Pendulum corrections to  $K_0$

Here, we indicate changes to the  $K_0$  which was found based on a perfect rectangular solid pendulum with dimensions indicated in table 3. Two pendulums were used in the course of our work, one with fibres 1 and 2, and a second with fibre 3. The effective characteristics of the first

**Table 5.** Corrections to  $K_0$  associated with the fibre 1 pendulum. Corrections reflecting differences in pendulums are to be incorporated in the run-dependent quantity  $S$ .

basis of change	$\Delta K$ (ppm)	uncertainty (ppm)
pendulum width	0	0.4
height	0	0
thickness	0	2.7
coating	−1.4	0.7
fibre attachment ferrule	−11.9	2.0
attachment screw and its glue	−3.0	0.7
chamfers	30.0	0.5
total $\Delta K$ and uncertainty	13.7	3.6

**Table 6.** ppm corrections to  $S_0$  depending only on torsion fibre and data year.

basis of $\Delta S$	fibre 1	fibre 2, y2000	fibre 2, y2002	fibre 3
pendulum version <sup>a</sup>	0	0.3	0.3	103.4 ± 1.8
mean rod length <sup>a</sup>	0	0	−2.6	−2.6
rod–ring tensioner <sup>a</sup>	0	0	−5.3	−5.3
Kuroda anelasticity correction <sup>b</sup>	−3.3 ± 1.7	−1.5 ± 0.8	−1.5 ± 0.8	−1.7 ± 0.9
ring configuration <sup>c</sup>	0	0	0	2.5
pendulum tilt	1 ± 1	1 ± 2	1 ± 2	2 ± 2
pendulum horizontal displacement	0 ± 0.5	0 ± 0.5	0 ± 0.5	−11 ± 4.0
pendulum vertical displacement	0 ± 0.5	0 ± 0.5	0 ± 0.5	0 ± 0.5
pendulum $\phi_0$ <sup>d</sup>	1 ± 1	1 ± 1	1 ± 1	1 ± 1
total $\Delta S$	−1.3 ± 2.3	1.8 ± 2.5	−6.1 ± 2.5	88.3 ± 5.1

<sup>a</sup>The uncertainty contributions for these  $\Delta S_0$  are included in  $K$ , so that in most cases no additional uncertainty need be added here.  
<sup>b</sup>The Kuroda corrections are based on zero torsional amplitude  $Q^{-1}$  values, see §1c.  
<sup>c</sup>A ring configuration  $S$  correction is applied explicitly only to data taken using fibre 3. Its uncertainty is included in the statistical uncertainty for  $S$  (fibre 3). The value of the correction depends on the choice of the multi-stage data averaging protocol, see §6a. The value here is found with the protocol we favour.  
<sup>d</sup> $\phi_0$  is the misalignment angle between the pendulum equilibrium axis and the source mass symmetry axis.

pendulum when used with fibres 1 and 2 differed slightly because of differences in the length of their ferrule linking the fibre to the pendulum. Table 5 shows corrections for the pendulum as hung for fibre 1. Corrections for the differences in  $q_{22}/I$  for the pendulums used with fibres 2 and 3 are applied to  $S_0$ .

(c) Corrections to  $S_0$

Some of these corrections vary only with the fibre used, others also depend on data year, torsional amplitude and/or on environmental parameters measured at the time of a particular  $S$  data point within a run. Table 6 shows corrections depending on torsion fibre and data year.

## (i) Corrections for pendulum misposition or misalignment

*Horizontal pendulum displacement from the source mass midpoint.* The  $G$  measurement is remarkably insensitive to such displacement—a horizontal misplacement as great as 10 mm requires a correction of less than 4 ppm for data taken at our torsional amplitudes between 2 and 8 radians. Horizontal displacement was measured to a few tenths of a millimetre by comparing torsional frequency measured when a 7 kg copper mass is suspended first on one side of the pendulum and then on the opposite side at the same radius. These frequencies should be equal when the pendulum is centred, as the frequency shift from the dominant  $m = 2$  coupling is proportional to  $\sin(2\theta)$ , where  $\theta$  is the angular orientation of the source mass. For all data taken with fibres 1 and 2, horizontal misposition was well under a millimetre, requiring no  $G$  correction. However, in preparing to take data with fibre 3, it seems certain that the ring transport turntable was translated in the wrong direction to correct for a measured 4.1 mm pendulum misposition, resulting in a 9.3 mm pendulum offset. This required a 10 ppm correction to  $S$  for fibre 3.

*Vertical pendulum displacement.* Here, a vertical misplacement of up to 7 mm produces  $G$  error less than 1 ppm. The vertical displacement of the pendulum relative to the source mass axis was measured using the same copper mass, placed at a series of heights to find the height at which the pendulum's frequency shift was an extremum. This showed that the vertical misplacement of our pendulum (after adjustment) was never greater than about 1 mm for all data used in our analysis, thus requiring no  $G$  correction.

*Pendulum rotation about its vertical axis.* As discussed in §4c, an angle  $\phi_0$  between the pendulum's equilibrium symmetry axis normal to its face and the symmetry axis of the ring/rod system requires a ppm correction  $+2\phi_0^2$  to be applied to  $S_0$ , where  $\phi_0$  is in milliradians. The uncertainty in this correction is  $4\phi_0\delta\phi_0$ , where  $\delta\phi_0$  is the uncertainty in  $\phi_0$  in milliradians. The orientation of the dewar was adjusted, so that measured values of  $\phi_0$  were well below 1 mrad for all data runs used in our analysis, thus requiring corrections less than 1 ppm. The contribution to the uncertainties in  $\delta\phi_0$  from error in angular calibration of the ring transport detente positions (§2a) was less than  $20\ \mu\text{rad}$ , contributing a  $G$  uncertainty of less than 0.1 ppm.

*Pendulum rotation about horizontal axes.* A rotation of the pendulum about an axis normal to its plane has negligible effect on  $G$ . However, a rotation about the horizontal axis in the pendulum's plane, producing a tilt  $\delta\theta$  away from vertical, requires a ppm  $G$  correction  $2(\delta\theta)^2$ , where  $\theta$  is expressed in milliradians. The required correction was 1–2 ppm, depending on the fibre.

## (ii) Corrections for fibre temperature variation

Particularly in data taken in y2002, we observed a correlation between the temperature measured at the fibre suspension point and the orientation of the source mass, revealed as values of  $T_{aba}$  defined as the difference between  $T$  measured for one source mass orientation minus the average of  $T$  measured in the immediately preceding and following (opposite) orientations. This was traced to an electronic coupling between a cable associated with the temperature control system and a cable associated with source mass transport. To correct for this we used measurements of the sensitivity of the pendulum period to temperature variation together with observed  $T_{aba}$ -values. The uncertainty in this correction was a significant contributor to our uncertainty budget: 3 ppm for fibres 1 and 2, and 7 ppm for fibre 3. Data associated with a  $T_{aba}$  greater than  $250\ \mu\text{K}$  were rejected.

## (iii) Corrections for air density and source mass temperature variation

Air pressure and source mass temperature (assumed equal to air temperature) were continuously monitored. A correction for expansion of the source mass rings and rods was based on expansion coefficients  $16.7 \times 10^{-6}$  per  $^\circ\text{C}$  for copper and  $5.5 \times 10^{-7}$  per  $^\circ\text{C}$  for fused silica, implying  $G$  sensitivity  $-31.0$  ppm per  $^\circ\text{C}$ . We estimated an uncertainty in  $G$  of 1.5 ppm associated with uncertainty in ring temperature measurements. Air density was based on  $0.0011592\ \text{g cm}^{-3}$  at temperature  $20^\circ\text{C}$  and air pressure 975 mbar, corrected for measured temperature and pressure,

assuming 0% relative humidity for our arid environment. We did not monitor humidity. Had 100% relative humidity been assumed, our resulting  $G$ -values would have differed by about 1.7 ppm.

## (d) Corrections for $m = 6$ and non-signal torques

### (i) $m = 6$ signal torque

There is a small amplitude-dependent correction to  $S_0$  from the  $\beta_6$  coefficient in equation (4.1) which is generated by the source mass. The ppm corrections for data taken near torsional amplitudes 0.26, 2.57, 4.2, 5.8 and 7.4 are given, respectively, by 5.6,  $-1.4$ ,  $-1.0$ ,  $-0.8$  and  $-0.6$ . The uncertainty in these corrections is negligible.

### (ii) Torque coefficients $b$ , $k_2$ , $k_3$ , $k_{ss}$ , $\alpha_1$ , $\beta_1$ , $\alpha_2$ and (non-signal) $\beta_{2ns}$

To first order, these constant torque coefficients in equation (4.1) have no effect on the change in torsional frequency when the sign of the signal  $\beta_{2s}$  is reversed. However, except for  $b$ , in second order they do have a marginally significant effect. To evaluate these effects, we devoted much effort to determining the values of these torque parameters for each of the three fibres. We then used each of these parameters in a numerical integration of equation (4.1), fitting the resulting oscillatory function in the same way as we fit real data, thereby determining each parameter's effect on the frequency change when the sign of the signal  $\beta_{2s}$  is reversed.

*Elastic fibre torques.* The nonlinear elastic coefficients  $k_2$  and  $k_3$  are determined, respectively, from the measured amplitude dependences of the  $\cos(2\omega t)$  and  $\sin(3\omega t)$  harmonics in equation (4.2). This measurement was made with very high precision for a fibre like our fibre 1 (20  $\mu\text{m}$  as-drawn CuBe fibre) in our early studies [5,6].  $k_3$  was determined with less precision for fibre 2 using our  $G$  data, and for fibre 3 was scaled from early tests using a 50  $\mu\text{m}$  Al5056 fibre to a value for our 25  $\mu\text{m}$  Al5056 fibre using the scaling relation  $k_3/k_1 \propto d^2/\ell^2$ . As the measured  $k_2$  for fibre 1 was found to affect the  $G$  signal by less than 0.05 ppm, we felt safe in taking  $k_2$  for fibres 2 and 3 to be equal to that for fibre 1.

*Stick-slip fibre torque.*  $k_{ss}$  for each fibre type was determined from the stick-slip relation  $k_{ss}/k_1 = (3\pi/8)(dQ^{-1}/dA)$  as discussed in §1c.

*Magnetic torques.* The  $m=1$  terms proportional to  $\alpha_1$  and  $\beta_1$  in equation (4.1) arise predominantly from magnetic couplings to the pendulum. We must distinguish three types of such coupling: (a) from magnetic moments of the source masses, (b) from fixed external fields, and (c) from magnetic fields generated within the dewar. Couplings of type a and b are reduced by the magnetic shielding described in §2f. Couplings of type b and c are not modulated by the source mass motion, and thus contribute to modulated frequency shift only through the sort of second-order effect generated by  $k_3$  and  $k_{ss}$ . The effect of type a couplings was found to be negligible by first monitoring the change in magnetic field generated by the source masses as they cycled between their two positions, and then measuring the sensitivity of pendulum oscillation frequency to a modulated field produced with a rotating bar magnet at the distance of the source mass. Type b couplings were evaluated by measuring the  $m=1$  variation of the pendulum's period as the dewar and its contents were rotated between stations at  $45^\circ$  intervals. Thus, values or limits of both  $\alpha_1$  and  $\beta_1$  from type a and b couplings are determined.  $\beta_1$  from type c coupling is determined from fitting the amplitude dependence of the pendulum's frequency averaged over ring position after removing the contribution of the measured  $k_3$  and  $k_{ss}$  values.  $\beta_1$  was found to be very small for fibre 3, but significant for fibres 1 and 2.  $\beta_1$  for fibres 1 and 2, which used a different pendulum from that used for fibre 3, was found to have equal magnitude but opposite signs for those two fibres. This we believe is because when the pendulum was hung with fibre 2 it must have been rotated  $180^\circ$  relative to its orientation when supported by fibre 1. Unfortunately, we have no direct information on the value of  $\alpha_1$  from type c couplings, but were able to put an 87% confidence limit on its value based on the known value of  $\beta_1$ . The sensitivity of measured  $G$  to  $\alpha_1$  is extremely small.

**Table 7.** Estimated torque coefficients in equation (4.1), expressed as ratios to  $k_1$  or to the signal magnitude  $\beta_{2S}$ .  $\beta_{2NS}$  is the contribution to  $\beta_2$  from non-signal fields.

fibre	$10^7 k_2/k$	$10^8 k_3/k$	$10^7 k_{ss}/k$	$\alpha_1/\beta_{2S}$	$\beta_1/\beta_{2S}$	$\alpha_2/\beta_{2S}$	$\beta_{ns}/\beta_{2S}$
1	$3.2 \pm 0.3$	$-3.7 \pm 0.4$	$8.0 \pm 0.8$	$0 \pm 2$	$0.4 \pm 0.2$	$0 \pm 0.3$	$0 \pm 0.1$
2	$3 \pm 3$	$-3.7 \pm 4$	$16.4 \pm 2$	$0 \pm 2$	$-0.4 \pm 0.2$	$0 \pm 0.3$	$0 \pm 0.1$
3	$3 \pm 3$	$-6.0 \pm 6$	$3.1 \pm 0.3$	$0 \pm 0.3$	$0.05 \pm 0.02$	$0 \pm 0.4$	$0 \pm 0.1$

**Table 8.** ppm corrections to  $S_0$  associated with torque coefficient values in table 7. These depend on torsional amplitude  $A$ ; values are shown for two of the five amplitudes at which data were acquired—these are typical of values found at the other three amplitudes. Values and their uncertainties are rounded to 0.1. The  $k_2$ -values in table 7 were found to have negligible effect on  $S_0$ .

fibre	$A$ (rad)	$dS(k_3)$	$dS(k_{ss})$	$dS(\alpha_1)$	$dS(\beta_1)$	$dS(\alpha_2)$	$dS(\beta_{ns})$	total
1	2.57	$0 \pm 0$	$-0.1 \pm 0$	$0 \pm 0.6$	$-2.5 \pm 1.3$	$0 \pm 0$	$0 \pm 1.2$	$-2.5 \pm 1.9$
1	7.4	$-1.0 \pm 0.1$	$-1.5 \pm 0.2$	$0 \pm 0.4$	$-2.4 \pm 1.3$	$0 \pm 0$	$0 \pm 4.9$	$-4.9 \pm 5.1$
2	2.57	$-0.2 \pm 0.2$	$-0.4 \pm 0$	$0 \pm 0.4$	$2.5 \pm 1.3$	$0 \pm 0$	$0 \pm 0.9$	$1.9 \pm 1.6$
2	7.4	$-3.8 \pm 3.8$	$-3.2 \pm 0.3$	$0 \pm 0.1$	$0.9 \pm 0.4$	$0 \pm 0$	$0 \pm 3.2$	$-6.1 \pm 3.9$
3	2.57	$0 \pm 0$	$0 \pm 0$	$0 \pm 0$	$-0.1 \pm 0.1$	$0 \pm 0$	$0 \pm 0.6$	$-0.1 \pm 0.6$
3	7.4	$-1.3 \pm 0.4$	$-0.4 \pm 0$	$0 \pm 0$	$0.2 \pm 0.1$	$0 \pm 0$	$0 \pm 0.2$	$-1.5 \pm 0.5$

*Gravitational couplings.* Next, consider  $\alpha_2$  and  $\beta_{2NS}$ , where  $\beta_{2NS}$  is the part of  $\beta_2$  which is not generated by the source masses. These torque terms are generated by gradients in the gravitational field generated by fixed mass distributions. They are generated (i) by masses external to the cryostat and dewar, and (ii) by masses associated with the cryostat and dewar. In both cases, the effect on torsional frequency change when the source masses move is only of second order, as from  $k_2$  and  $k_{ss}$ . The contributions from type a couplings are determined from  $m=2$  modulation of the torsional frequency in the same test runs that determined the  $m=1$  modulation from magnetic couplings, in which the dewar was rotated in  $45^\circ$  increments. We have no direct knowledge of the type b couplings, but they should be negligible, because all components of the pendulum’s cryostat and dewar with significant mass have a precise fourfold symmetry and thus should generate no field gradient ( $m=2$  coupling).

We have no satisfactory way to estimate the effect of possible electrostatic couplings, except to note that such couplings must be uncorrelated with source mass position in the absence of source-mass-induced instrument tilt. The symmetry of the source mass configuration and the design of apparatus make such source-mass-induced tilt virtually impossible. The closest distance from the pendulum to the structure above and to its side was about 6 cm, and to the structure below about 2.5 cm. The resistance from pendulum to ground was verified *in situ* to be small. Ultimately, the only bounds on electrostatic effects come from the level of consistency between data collected at different times and especially at different torsional amplitudes.

Table 7 gives the values of torque coefficients found with the studies described in this section, and table 8 shows corresponding amplitude-dependent corrections to the measured  $G$  for a sampling of amplitudes. Our final measured  $G$  is based largely on data taken at a torsional amplitude near 2.57, where the required amplitude-dependent corrections are relatively lower. The net corrections  $\delta G$  for these torque components, to be added to the final  $G$ -values found for fibres 1, 2 and 3, are respectively  $(-2.6 \pm 2)$ ,  $(1.9 \pm 2)$  and  $(-0.7 \pm 1)$  ppm.

**Table 9.** Full systematic ppm uncertainty table. The field source and associated uncertainties are common to data using fibres 1, 2 and 3. Pendulum no. 1 uncertainty is common to data using fibres 1 and 2. The remaining uncertainty contributions in the table are largely uncorrelated.

uncertainty source	fibre 1	fibre 2	fibre 3
field source metrology (table 4)	7.8	7.8	7.8
pendulum metrology (table 5)	3.6	3.6	3.6
correlated subtotals	8.6	8.6	8.6
sum of contributions from table 8 <sup>a</sup>	2.3	2.5	5.0
non-signal torques	3	3	15
fibre temperature variation	3	3	7
field source temperature	1.5	1.5	1.5
air density determination	1.3	1.3	1.3
turntable inaccuracy	1	1	1
largely uncorrelated subtotal	5.3	5.4	9.0
total	10.1	10.2	12.4

<sup>a</sup>These uncertainties are for the total corrections arising from the torque coefficients referenced in table 8.

(e) Collecting all systematic uncertainties

Table 9 presents a full list of known significant systematic uncertainties in our *G* measurement.

6. Data collection and analysis

A total of about 2500 h of *G* data were collected in y2000, y2002, y2004 and y2006, in addition to many hours devoted to systematic error investigations. Data taken in y2004 proved to be exceptionally noisy, probably for two reasons: a leak that had developed in the evacuated thermal insulation gap between the outer and inner walls of the dewar, and an untightened screw in the cryostat inner structure. It was decided to reject all data taken in y2004. The faulty dewar was replaced before taking y2006 data. Characteristics of the y2000, y2002 and y2006 data are indicated in table 10.

Prior to each data run, the pendulum oscillation amplitude was raised to typically 25 mrad above a target mean amplitude, by rotating the dewar in a sequence of alternate directions. In the course of a run, the amplitude decayed an amount which varied with run duration, pendulum *Q* and amplitude, but was of the order of 50 mrad. In each run, the source mass was positioned alternately at orientations 90° apart, where a ‘dataset’ of *N* pendulum oscillation cycles was completed. *N* was fixed for a given run, but differed during various periods of our work, ranging from 12 to 24. The time spent at each source mass orientation averaged about 44, 37 and 23 min for fibres 1, 2 and 3, respectively. The average run duration was about 21 h. After a run was started all humans left the underground laboratory.

(a) Data processing stages

Data were processed in stages we denote *a*, *b*, *c*, and 1–5 as follows.

*Stage a.* Detector transit times within each source mass position dataset are fitted to determine an average torsional period *P* and average torsional amplitude *A*. The fit yields *P* and its calculated uncertainty  $\delta P$  for each dataset (ring orientation). This yields a total of 3690 *P*-values.

*Stage b.* The *P*-values for each run are divided into group 1 found at one source mass orientation and group 2 found at the other orientation. Each group is fitted to a quadratic function of time,

**Table 10.** Data characteristics.  $T$  (fibre) is the mean temperature measured at the upper suspension point of the fibre.  $Q$  is the value measured at torsional amplitude  $A \approx 2.6$  radians. Pendulum 1b differs from 1a only in the length of the fibre attachment ferrule.

group	dates	fibre	pendulum	period (s)	$Q$	$T$ (fibre; K)	runs	hours
1	9–11/2000	1	1a	135	82 000	2.65	23	604
2a	12/2000	2	1b	130	120 000	4.6	9	135
2b	3–5/2002	2	1b	130	120 000	2.75	9	705
3	3–5/2006	3	2	113	182 000	3.0	36	683

yielding  $F1$  and  $F1$ . The mean of  $F1$  and  $F1$  is then subtracted from the  $P$ -values in each group, and the two results are combined to form a single set which retains the signal modulation but removes to quadratic order secular drift of the fibre's torsion constant. In the fit process, about 2% of the  $P$ -values are rejected as outliers and replaced with 'artificial' values constructed using the fit to the remaining points. For use in finding  $\Delta\omega^2$  in further stages, a constant value of  $P$  equal to the mean of the first two pre-fit values is added to each point in the background-subtracted data.

*Stage c.* The  $P$ -values for each run are converted to  $\omega^2$  and used to form a set of overlapping  $\Delta\omega_{aba}^2$ -values defined as  $\omega_i^2 - (\omega_{i-1}^2 + \omega_{i+1}^2)/2$ . Then, an  $S_0$ -value is obtained as

$$S_{0,aba} = \frac{\Delta\omega_{aba}^2}{2J_1(2A_i)/A_i + (2J_1(2A_{i-1})/A_{i-1} + 2J_1(2A_{i+1})/A_{i+1})/2}. \quad (6.1)$$

This corresponds to the  $S_0$  defined in equation (4.14) in §4*d*, but with the decay in amplitude taken exactly into account. Propagating the uncertainties assigned to the periods  $P$  from which the  $S_{aba}$  is formed yields an uncertainty  $\delta S$  for each  $S_0$  thus found. At this point, the various corrections to  $S$  discussed in §5*c* are applied to obtain  $S_{aba}$ .

*Stage 1.* Here, the  $S_{aba}$ -values and their uncertainties for each run are combined with a weighted or unweighted average (as discussed in §6*c*) to form an  $S(\text{run})$  and  $\delta S(\text{run})$ , along with a  $\chi^2/\text{d.f.}$  for the average where d.f. denotes degrees of freedom.

*Stage 2.* Here, the weighted average and  $\chi^2/\text{d.f.}$  is found for  $S(\text{run})$  values corresponding to runs with the same fibre, nominal torsional amplitude  $A$ , and ring configuration, forming a set of  $S$ -values which we denote  $S(f, A, R)$  with  $f$  denoting fibre and  $R$  denoting one of the four ring configurations discussed in §3*a*.

*Stage 3.* Here, weighted averages over  $A$  are made of  $S(f, A, R)$ -values with the same  $f$  and  $R$ , yielding  $S(f, R)$ .

*Stage 4.* Here, an *unweighted* average is made of  $S(f, R)$  over  $R$  to yield  $S(f)$  for fibres 1 and 2. An unweighted average helps here to yield an  $S$ -value as close as possible to what would have been obtained with an idealized source mass shape. A fibre 3  $S$ -value was found using only  $R$  configuration no. 1. We correct it by adding to it  $\Delta S \equiv \bar{S} - S_1$ , where  $\bar{S}$  is the average of  $S(f, A = 2.6, R)$  over  $R$  and  $S_1$  is  $S(f, A = 2.6, R = 1)$  with  $f$  either fibre 1 or 2. In practice, we base our correction on the weighted average of  $\Delta S$  found with fibres 1 and 2.

*Stage 5.* Here, we have  $S(f)$  for all three fibres, and consider trying to average over  $f$  to find a single best  $S$ . As the uncertainties  $\delta S$  have complex correlations, the safest thing to do here would be to take the final  $S$  to be the unweighted average of the  $S(f)$ -values, with an uncertainty equal to the mean of the  $\delta S(f)$ -values to represent a limit on what  $\delta S$  might be.

## (b) Data rejection

At the beginning of stage 1 processing, there were a total of 1669  $S_{aba}$ -values. We deleted from our dataset the first three runs made in y2000 because of large  $\phi_0$  value and lack of fibre temperature data. We then deleted the first three  $S_{aba}$  associated with each run, so that the analysed portion of the run data would suffer minimally from possible fibre relaxation noise immediately following



**Table 11.** The components of the ppm uncertainty assigned to  $G$ -values determined using each of the three fibre types. Fibre 1 was as-drawn CuBe, fibre 2 was heat-treated CuBe and fibre 3 was as-drawn Al5056.

component	fibre 1	fibre 2	fibre 3
statistical	7.7	15.7	11.3
systematic	10.1	10.2	12.4
analysis method	6.9	12.0	10.2
quadrature sum	14.5	22.2	19.6

the pumping up of torsional amplitude before each run. Then, we deleted runs with fewer than three remaining  $S_{aba}$ -values, leaving a total of 1322  $S_{aba}$ -values. Then, 149 values were deleted because of excessive ring swing following ring transport for the fibre 3 data (the ageing turntable bearing was giving problems, later reduced with maintenance). An additional 87  $S_{aba}$ -values were dropped because of excessive fibre ' $T_{aba}$ ' correlation of fibre temperature as measured at its suspension point with source mass orientation. We were left with 1085  $S_{aba}$ -values.

### (c) Robustness test of the stage 1–3 averaging process

There are a number of choices that may be made in this sequence of procedures, and it is important to test the robustness of our choice. An important observation was that the  $\chi^2/\text{d.f.}$  for the averages made of  $S_{aba}$  within runs to get  $S(\text{run})$  were exceptionally high, with median value 14. Clearly, there was a source of noise introduced between period measurements that was much greater than could be attributed to uncertainty in the individual period measurements themselves. Similarly, at later stages in the processing we encountered  $\chi^2/\text{d.f.}$  values that were not as extreme but uncomfortably high. The processing choices we explored varied as follows:

1. At stage 1, we could use averaging that was (i) weighted, (ii) unweighted, or (iii) weighted if an Allan variance plot of the data indicated white noise and unweighted if otherwise. The Allan variance plots indicated that 73 of the runs were roughly consistent with white noise, while seven were not.
2. In averages made at stage 2 and stage 3, we could respond to high  $\chi^2/\text{d.f.}$  by expanding uncertainties by a factor making (i) the Birge ratio  $\sqrt{\chi^2/\text{d.f.}} = 1$ , (ii) the probability  $p$  value = 0.05, or (iii)  $p = 0.01$ —in cases a, b and c expanding respectively only if the initial Birge ratio were  $>1$ ,  $p < 0.05$  or  $p < 0.01$ .
3. At each stage we could choose: (i) to delete no outlier data, or, (ii) and (iii), use one of two different outlier deletion criteria.

We did a full analysis for stages 1–4 using all combinations of these options, a total of 27 variants. The 27 different resulting  $G$ -values for fibres 1, 2 and 3 varied, respectively, over a max–min range of 14, 24 and 20 ppm, with variation standard deviations of 5, 6 and 6 ppm.

We opted to use options 1b (unweighted stage 1 averaging), 2a (Birge ratio uncertainty expansion), and an outlier identification protocol which rejected 2% of  $S_{aba}$  outlier values at stage 1, 3 of 81 runs at stage 2, and no data at stage 3. To the  $G$  uncertainties for each fibre, we add in quadrature an 'analysis method' component equal to half of the max–min spread of  $G$ -values found for that fibre.

Table 11 indicates the uncertainty components we assign for the statistical, systematic and 'analysis method' contributions, and their quadrature sum, for  $G$ -values determined using each of our three fibre types.

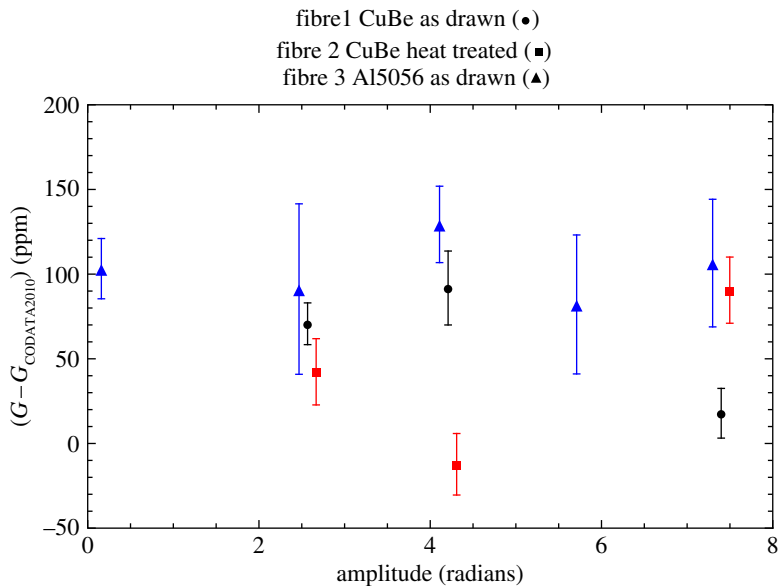


**Figure 5.**  $G$ -values for the three fibres relative to CODATA2010 in ppm, as determined at each of the five torsional amplitudes at which the pendulum operated. Data near 0.26 and 5.8 radians were obtained only with fibre 3. Error bars represent statistical contributions only. (Online version in colour.)

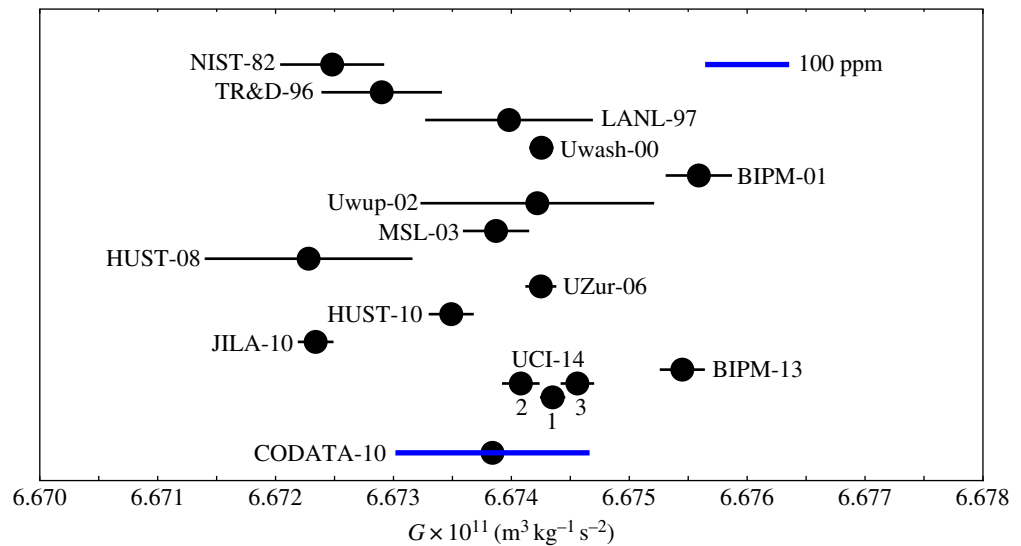


**Figure 6.**  $G$  measurements reported in recent years. The designations and  $G$ -values correspond to those recorded in the 2010 CODATA report [8] with the exception of BIPM-13 [9] and the results reported in this paper, denoted here as UCI-14. The fibres used in obtaining the three UCI values are indicated below their position in the plot. Fibre 1 was as-drawn CuBe, fibre 2 was heat-treated CuBe, and fibre 3 was as-drawn Al5056. (Online version in colour.)

## 7. Conclusion

Figure 5 displays values of  $G$  found in this work using data taken with the three fibres at different torsional amplitudes.

The final  $G$ -values and uncertainties for the three fibres are as follows:

Determined using fibre 1:  $6.67435(10) \times 10^{-11} \text{ m}^3 \text{ kg}^{-1} \text{ s}^{-2}$  14 ppm.

Determined using fibre 2:  $6.67408(15) \times 10^{-11} \text{ m}^3 \text{ kg}^{-1} \text{ s}^{-2}$  22 ppm.

Determined using fibre 3:  $6.67455(13) \times 10^{-11} \text{ m}^3 \text{ kg}^{-1} \text{ s}^{-2}$  20 ppm.

Unweighted average:  $6.67433(13) \times 10^{-11} \text{ m}^3 \text{ kg}^{-1} \text{ s}^{-2}$  19 ppm.

We have no explanation for the inconsistency of these results. We speculate that the  $G$ -value determined with the Al5056 fibre 3 may be the least subjected to fibre-associated systematic error because of its higher  $Q$ .

The correlations among the uncertainty components of the three results are complex. To assign an uncertainty to the unweighted average of the  $G$ -values, we used the average uncertainty of the three  $G$ -values, corresponding to 100% correlation—the maximum that could result from an analysis taking full account of the correlations of the three  $G$  uncertainties.

The UCI  $G$  results are displayed in figure 6 along with recent  $G$ -values found by other workers.

**Acknowledgements.** We thank the Pacific Northwest National Laboratory (PNNL), and particularly Roy Gephart, for hosting and supporting our experimental site; Paul Dunn, Haskell Sheinberg and Bill Baker and the Los Alamos National Laboratory for the source mass fabrication; Zeina Jabbour, Howard Harary, and Dennis Everett and NIST for ring mass and dimensional measurement; the many researchers, students and staff at UCI who contributed to this work over the past 18 years; and Terry Quinn, Clive Speake and Jun Luo for organizing the Royal Society conference which led to this paper. This research was conducted with funding from the National Science Foundation (including grant no. 0404514).

**Data accessibility.** Data from multiple data analysis stages of this  $G$  measurement are accessible at [www.webfiles.uci.edu/rdnewman/public](http://www.webfiles.uci.edu/rdnewman/public).

## References

1. Kuroda K. 1995 Does the time-of-swing method give a correct value of the Newtonian gravitational constant? *Phys. Rev. Lett.* **75**, 2796–2798. (doi:10.1103/PhysRevLett.75.2796)
2. Quinn TJ, Speake CC, Brown LM. 1992 Materials problems in the construction of long-period pendulums. *Phil. Mag. A* **65**, 261–276. (doi:10.1080/01418619208201522)
3. Gundlach JH, Merkowitz SM. 2000 Measurement of Newton's constant using a torsion balance with angular acceleration feedback. *Phys. Rev. Lett.* **85**, 2869–2872. (doi:10.1103/PhysRevLett.85.2869)
4. Newman RD, Bantel MK. 1999 On determining  $G$  using a cryogenic torsion pendulum. *Meas. Sci. Technol.* **10**, 445–453. (doi:10.1088/0957-0233/10/6/306)
5. Bantel MK. 1998 Anelastic behavior of a torsion pendulum with a CuBe fiber at low temperature. PhD thesis, University of California, Irvine, CA, USA.
6. Bantel MK, Newman RD. 2000 High precision measurement of torsion fiber internal friction at cryogenic temperatures. *J. Alloys Comp.* **310**, 233–242. (doi:10.1016/S0925-8388(00)01010-0)
7. Lebedev AB. 1996 Amplitude-dependent decrement to modulus defect ratio in breakaway models of dislocation hysteresis. *Phil. Mag. A* **74**, 137–150. (doi:10.1080/01418619608239694)
8. Mohr PJ, Taylor BN, Newell DB. 2012 CODATA recommended values of the fundamental constants. *Rev. Mod. Phys.* **84**, 1527–1605. (doi:10.1103/RevModPhys.84.1527)
9. Quinn T, Parks H, Speake C, Davis R. 2013 Improved determination of  $G$  using two methods. *Phys. Rev. Lett.* **111**, 101102. (doi:10.1103/PhysRevLett.111.101102)